Metals & corrosion

The role of the microstructural changes during induction preheating on the HAZ liquation cracking susceptibility of Ni-based superalloy

Łukasz Rakoczy[1,*] , Małgorzata Grudzień-Rakoczy[2], Bogdan Rutkowski[1], Rafał Cygan[3], and Anna Zielińska-Lipiec[1]

[1] *Faculty of Metals Engineering and Industrial Computer Science, AGH University of Kraków, Mickiewicza 30, 30-059 Kraków, Poland*
[2] *Łukasiewicz Research Network-Kraków Institute of Technology, Zakopiańska 73, 30-418 Kraków, Poland*
[3] *Investment Casting Division, Consolidated Precision Products Corporation, Hetmańska 120, 35-078 Rzeszów, Poland*

ABSTRACT

This work presents the influence of high-frequency induction preheating (900, 1000, 1100 °C) on liquation crack formation in the René 108 Ni-based superalloy. The investigation was divided into two parts: (1) characterization of the material's microstructure after preheating and (2) determining the influence of preheating on liquation cracking during autogenous gas tungsten arc welding. During preheating, the dissolution of γ' precipitates showed accelerated progress with increase in temperatures. This dissolution involved the continuous thinning of each precipitate, as well as more intricate mechanisms, such as splitting. The mean size of the secondary γ' decreased from 0.32 to 0.26 μm. In the heat-affected zone (HAZ) induced by welding, constitutional liquation of mainly γ' precipitates, with a contribution of $M_{23}C_6$ carbides and M_5B_3 borides, was observed. The formation of a thin non-equilibrium liquid film along high-angle grain boundaries led to the crack initiation and their further propagation during cooling. The eutectic γ–γ' re-solidification products were visible on the crack edges independently of preheat temperature. Preheating at 900 °C decreased the length and amount of liquation cracks, while preheating at 1100 °C allowed to prevent them due to the liquid-healing effect.

Introduction

The use of welding in the joining of Ni-based superalloys during production, finishing of castings, and the repair of serviced components allow for reducing the overall cost of the final product [1–3]. However, superalloys in liquid form are characterized by high viscosity, which poses challenges in its spreading and wetting within the weld groove. The penetration depth does not increase proportionally with increase in

---

Springer

welding input energy [4]. The application of welding heat sources, including arc and concentrated sources (e.g., lasers, electron beams) for joining Ni-based superalloys is significantly restricted due to its susceptibility to hot, liquation and strain age cracking [5, 6]. The overall superalloys' weldability is commonly evaluated based on the total Al and Ti concentration. These elements create and influence volume fraction of the γ' phase. When it exceeds 6 wt%, cracks can appear [7, 8]. In superalloys, with a low Al + Ti concentration, such a problem usually does not occur, and conventionally welded joints are characterized by sufficiently high strength and toughness directly in as-weld condition [9]. Many Ni-based superalloys are typically characterized by a complex chemical composition, necessitating the analysis of other elements present in the matrix to determine their effects of the material's weldability [10]. For numerous superalloys, these criteria can be ambiguous, signifying that additional factors must be considered before reaching a final weldability assessment. Previous analyses have found that preheating prior to welding can help to avoid issues, such as liquation cracking [11]. By preheating at a sufficiently high temperature, the volume fraction of the γ' phase can be reduced, in turn decreasing welding stresses. This furthermore facilitates minimizing or completely preventing adverse effects of constitutional liquation and modifying the amount of liquid alloy to initiate the self-healing effect. The influence of various aspects on hot cracking susceptibility in Ni-based superalloys included time–temperature parameters, preheating sources and welding methods. The SX PWA1480 superalloy autogenously welded via electron beam (EB) and an Nd-YAG laser, showed high susceptibility to hot solidification and liquation cracks [12]. To reduce this susceptibility, preheating to 500 °C was proposed. During EB welding, the preheating temperature was reached with a defocused beam. Maintaining the following welding parameters: crystallographic direction consistent with [100], speed 4.3 or 6.3 mm/s, accelerating voltage 100 kV and current in the range of 3–13 mA, allowed to obtain crack-free joints. When the welding speed was increased to 42 mm/s, cracks formed again. Upon pulsed laser welding, the preheating temperature was achieved using an additional gas torch. A specific set of parameters was chosen to eliminate hot cracks: welding speed of 2.1 or 4.2 mm/s, pulse frequency of 100 pulses/s, pulse length 1–3 ms and power 90–240 W. Local melting with an EB or laser

disrupted the pre-weld crystallographic orientation of the SX PWA1480 superalloy. The weld zone exhibited a characteristic cell-dendritic structure, with crystallites nucleating epitaxially on the partially melted edges. Some welds exhibited deviation from the [001] direction, which can be induced by factors, such as concentration supercooling or heat dissipation. Such grains are referred to as stray grains and have been identified as strong crack initiators. Liquation cracking was not observed. The beneficial influence of preheating in reducing susceptibility to solidification and liquation cracking was also observed during multipass cladding using a Nd-YAG laser on IN738LC superalloy powder [13]. The powder was applied onto a stainless-steel plate, which was inductively heated to 800, 900 and 1050 °C. Following the first pass, the IN738LC became a substrate for the next passes. The parameters remained constant for each heating temperature: 900 W, cladding speed of 240 mm/min and beam diameter of 1 mm. Preheating to 800 °C resulted in a fourfold reduction in the overall crack length. At 900 °C, it exceeded a tenfold reduction. Preheating to the highest temperature of 1050 °C eliminated hot cracking altogether. Based on the analysis of the fiber laser surfacing process of the DZ4125 superalloy powder on DZ4125 (in as-cast condition), a correlation between the linear energy and susceptibility to cracking was observed [14]. Single bead-on-plate with different linear energies of 50, 70, 90, 130 or 150 J/mm was applied on an inductively preheated plate (500 °C). The susceptibility to liquation cracks was defined as the parameter CR = N/L, where N is the number of cracks measured in three cross sections and L is the bead length. With the increase in linear energy (from 70 J/mm), the CR parameter decreased, reaching 0 for 150 J/mm. Based on the microstructure, it was found that the key to reducing the number of cracks in the heat-affected zone was the self-healing of micro-fissures by the liquid. Suharno [15] did not receive positive results when using resistance preheating to 200 °C (2 h holding time) during tungsten inert gas (TIG) repair welding of compressors made of superalloy IN792. Numerous liquation cracks were observed in the HAZ. However, further attempts to increase the temperature were carried out, so the effectiveness of this solution for the IN792 superalloy has not been fully verified.

The René 108 Ni-based superalloy, due to its complex chemical composition and high concentration of γ'-formers, is susceptible to liquation cracking [16].

Based on cracking mechanism analysis, it has been observed that preheating before welding can help to improve weldability. This work aims to reveal the role of induction preheat in reducing the susceptibility to liquation cracking formation in the heat-affected zone. To understand the behavior of complex Ni-based superalloys during autogenous welding with applied preheating, it is necessary to fully investigate their microstructural changes. Similar experiments have been carried out on only a few superalloys, and data about the René 108 is still missing. The presented results allow us to fulfill this gap in the literature.

Material and methodology

The chemical composition of the fully heat-treated (solution + aging) cast René 108 superalloy used in this study is shown in Table 1.

Two sets of specimens were prepared. The first set were used for preheating experiments, where 10 × 10 × 3 mm plates were inductively heated (Dacpol Ambrell Ekoheat device) at a rate of 150 °C/min and then held for 3 min at a set temperature T_0 (900, 1000, 1100 °C). Afterward, the samples were cooled in ice water to obtain a microstructure as close as possible to that at high temperature. Two independent pyrometers were used for temperature control (IRCON Modline). The second set of samples (90 × 20 × 10 mm) was prepared to evaluate the influence of the preheating temperature on the susceptibility to liquation cracking in the HAZ of the superalloy during GTA autogenous bead-on-plate welding (Fronius welding machine). The samples were placed in an inductive coil located in a cubic tank, which was filled with argon during the entire process (flow rate 20 l/min). The work involved welding with induction preheating to $T_0 = 900$, 1000 or

1100 °C. The heating rate and holding time were 150 °C/min and 3 min, respectively. The welding parameters are summarized in Table 2.

The cross-sectioned samples (from both sets) were subjected to standard metallographic preparation. They were mounted in resin, ground on SiC papers (from #120 to #4000) and polished on diamond suspensions (3 μm pre-polishing, 1 μm final) and silica oxide (0.06 μm). The samples were electrolytically etched in a 10% aqueous solution of oxalic acid. Microstructure observations were carried out via light microscopy (LM, LEICA DM 4000 M) and scanning electron microscopy (SEM, Phenom XL-ThermoFisher). An accelerating voltage of 20 kV was used together with a back-scattered electron detector (BSE). Focus was placed on identifying and assessing the stability of strengthening phases formed during preheating, as well as characterizing cracks and self-healed areas. The ImageJ software was employed for quantitative analysis of microstructural changes induced by preheating. SEM-BSE images were binarized and subsequently despeckle-filtered to remove minor noises. Microstructure quantitative analysis involved determining the relative volume fraction and size of γ′ phase precipitates in dendritic regions. The relative volume fraction (V_f) of γ′ precipitates was determined using the planimetric method. Following the Cavalieri-Harquet principle, the estimator of the relative volume occupied by the microstructure component (γ′) in the superalloy is the fraction of the area it occupies on a unit plane (1, 2). To determine the average volume fraction of γ′ precipitates, 10 images (× 20 k) of each sample was taken.

$$V_v = A_A \tag{1}$$

Table 1 Chemical composition of the René 108 Ni-based superalloy, wt %

Element	Cr	W	Co	Al	Ta	Hf	Ti	Mo	C	B	Zr	Ni	Others
Concentration	11.40	8.85	8.19	6.35	3.55	1.52	0.75	0.45	0.08	0.015	0.014	Bal	P-0.006 S-0.0002

Table 2 GTA autogenous bead-on-plate welding parameters

Parameter	Welding current DC (A)	Arc voltage (V)	Welding speed (mm/min)	Electrode	Electrode diameter (mm)	Flow rate in torch (l/min)	Torch distance (mm)
Value	50	12	180	W-2%Th	1.8	10	3

$$A_A = \left(\frac{\Sigma A_i}{A}\right) * 100\% \qquad (2)$$

where: V_v—relative volume, $\mu m^3/\mu m^3$; A_A—relative area, $\mu m^2/\mu m^2$; A_i—area of a single γ' precipitate, μm^2; A—total region area, $\mu m.^2$

For the stereological analysis of the γ' precipitates, it was assumed that they are cubic-shaped, and their size estimator D is the equivalent side d (edge length) equal to the square root of the precipitate area. Only precipitates in the dendritic areas with a surface area of 0.03–6.00 μm^2 were analyzed. At least 3000 γ' precipitates from each tested sample were investigated. The further observations were conducted using the JEOL JEM-200CX transmission electron microscope (TEM) and the FEI Titan3 Cubed G-2 60–300 high-resolution analytical TEM equipped with an EDX ChemiSTEM system. The preparation of thin foils included mechanical cutting of the samples and then grinding them on sandpaper to a thickness of about 40 μm. The samples were cut into 3-mm-diameter disks and subsequently dimpled on both sides using diamond suspension. The final step consisted of ion thinning (Ar +) using a Gatan Precision Ion Polishing System. To obtain thin lamellae from the grain boundaries in the heat-affected zone, samples were extracted using a ThermoFisher Scios 2 DualBeam FIB-SEM instrument. The process involved using a focused ion beam (FIB) with Ga + ions. The instrument was equipped with a field emission gun and a Ga + ion source. Subsequently, the extracted lamellae were ion polished until they reached a thickness less than 100 nm. Prior to analysis, the samples were subjected to plasma cleaning using a low-energy NanoMill 1040 device (Fischione) to remove surface impurities. The structure was imaged in bright and dark fields, including HAADF-STEM (High-Angle Annular Dark Field-Scanning-Transmission Electron Microscopy) observations. The fast Fourier transformation (FFT) method was used to create diffraction patterns. These images were then analyzed using the JEMS software. The distribution of alloying elements in the selected areas was determined via STEM-EDX microanalysis.

Results and discussion

Preheating-induced microstructural changes in dendritic regions and interdendritic spaces

The material was characterized by a typical cast microstructure with clearly visible dendritic regions and interdendritic spaces. In Fig. 1, the change in the morphology and size of the γ' precipitates in dendritic regions is shown. Two groups of γ' precipitates can be observed, i.e., large secondary γ' precipitates with relatively extensive interfacial boundaries, and finer cubic-like shaped ones. The two groups exhibit clear differences in the degree of dissolution. The larger ones gradually dissolve with increase in temperature. At 1100 °C, the size and number of large γ' phase precipitates significantly decreased. With increase in preheating temperature, the γ' precipitate volume fraction decreased, however, not linearly. At 900 °C, the volume fraction of the secondary γ' precipitates was about 51.9% (± 3.9%). As the preheating temperature increased, the volume fraction of the precipitates gradually decreased to about 34.4% (± 5.3%) at 1100 °C. The size of the cubic precipitates changed to a lesser extent. These observations indicate that the dissolution process does not occur by uniform size reduction ("thinning"), but by a more complex mechanism.

It was also observed that the dissolution process of large γ' secondary precipitates can occur by gradual splitting. This disintegration was also observed in other Ni-based superalloys strengthened by γ' precipitates characterized by a relatively high γ/γ' lattice misfit parameter [17, 18]. High elastic deformation energy can cause morphology instabilities of γ' precipitates characterized by a high misfit with the γ matrix, leading to their splitting into finer precipitates and the reduction of their total internal energy. Assuming the common rule that the precipitate's shape results only from the sum of elastic deformation energies, caused by the degree of misfit, and their interfacial energy, the splitting mechanism should not take place [19]. This is essentially due to the increase in precipitate interfacial energy caused by the increase in the interfacial area. However, the microstructure of the precipitates indicates that splitting took place, which confirms that there was an additional factor reducing the total energy despite the increase in interfacial energy. It was the energy of elastic interactions between the γ' precipitates [20]. The γ' phase precipitate size was expressed as the equivalent side of the square. The

Figure 1 Change in the γ' precipitates morphology and mean size in the dendritic regions after the preheating: **a–b** 900 °C; **c–d** 1000 °C; **e–f** 1100 °C.
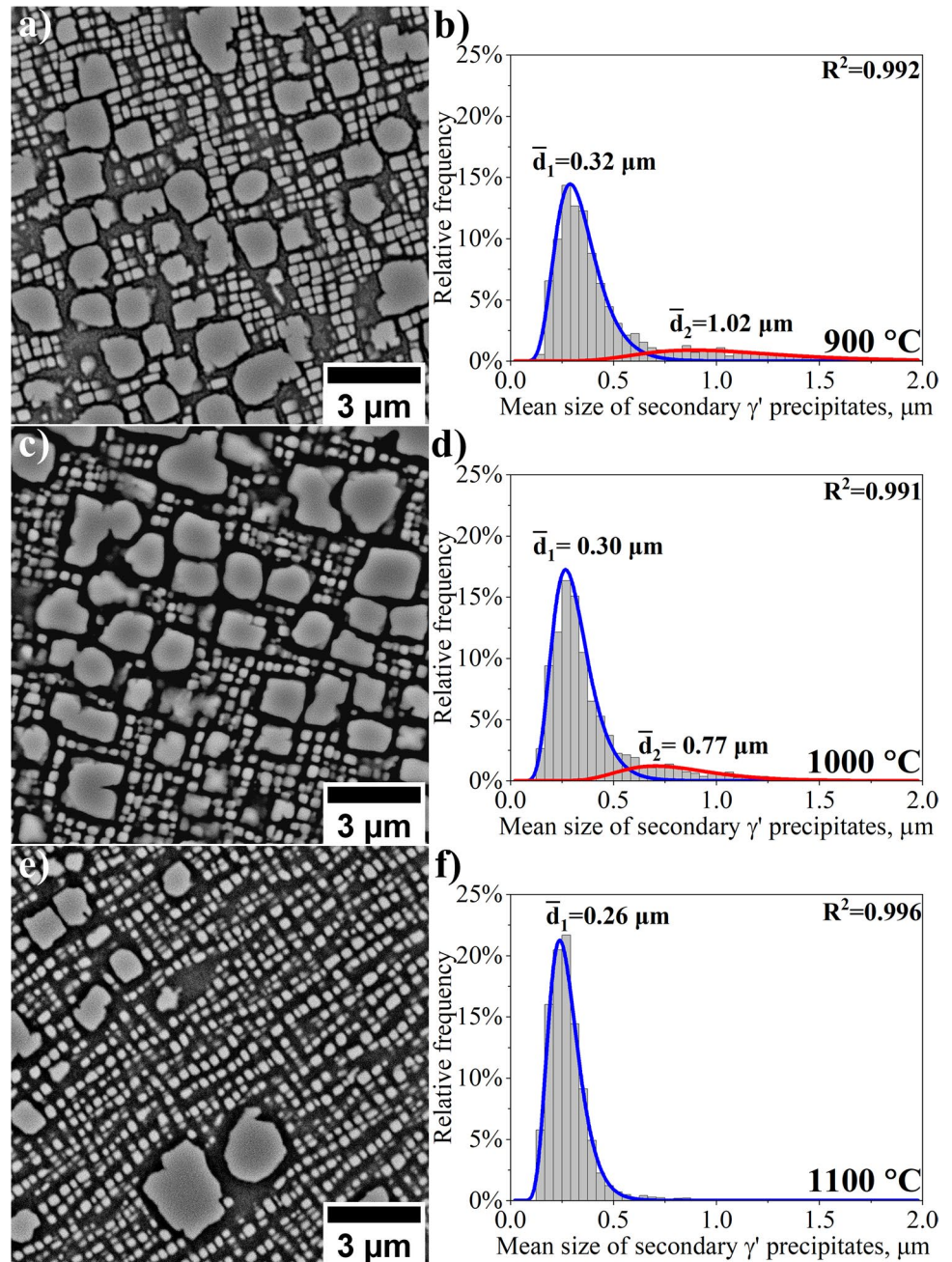
distribution of changes in the γ' precipitates' size with increase in preheating temperature is shown in Fig. 1. At 900 °C, two distribution curves were fitted (log-normal), obtaining mean values of $d_1 = 0.32$ μm and $d_2 = 1.02$ μm. At 1000 °C, the dissolution process began to dominate, which led to a decrease in precipitate average size, $d_1 = 0.30$ μm and $d_2 = 0.77$ μm. Preheating at 1100 °C caused a significant size decrease in the large secondary precipitates. The structure predominantly consisted of fine precipitates represented

by a single-size distribution. The presented data confirmed significant differences in the dissolution of cubic and large secondary γ' precipitates, with the former exhibiting only slight changes, highlighting their greater stability. In the second set of samples, there was a significant decrease in the size and number of precipitates. The morphology of the γ' precipitates and MC carbides in the interdendritic spaces and fine precipitates along the grain boundaries after the preheating cycle is shown in Fig. 2. The change
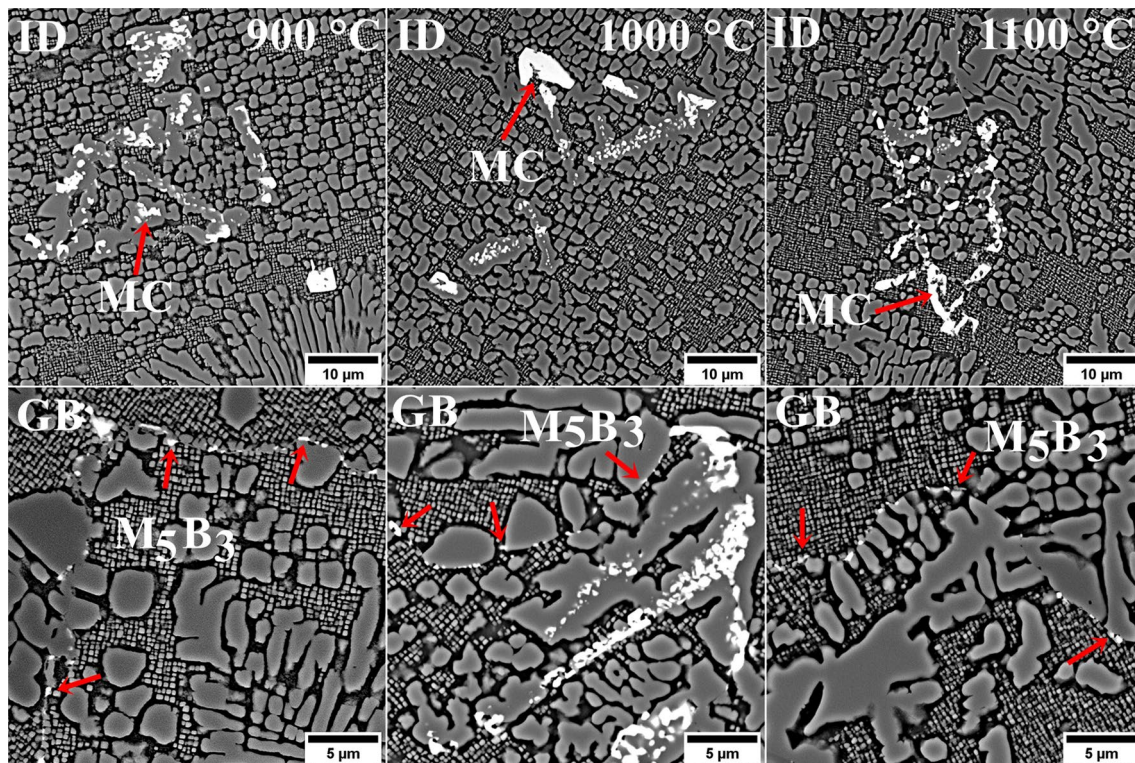
Figure 2 Change in the morphology of the γ' phase precipitates in the interdendritic spaces (ID) and grain boundaries (GB) after the preheating, SEM-BSE.

in γ′ precipitate morphology and size was induced by dissolution as a function of temperature; however, quantitative analysis of these changes was hindered due to the significant differences in precipitate size and morphology in their initial state. After preheating at 1100 °C, a significant portion of large secondary γ′ precipitates surrounding MC carbides was partially dissolved. The morphology of MC carbide precipitates did not significantly change, which suggests that their possible dissolution process could occur only locally at 1100 °C. The bright-phase precipitates strengthening the grain boundaries remained stable. Samples preheated to 1100 °C, in which the dissolution process was the most intensive, were subjected to TEM/STEM analysis to obtain more information on microstructure evolution. Numerous dislocations can be observed at the interfaces of the secondary γ′ with the matrix (Fig. 3a). The high temperature caused the dissolution of most of the large secondary γ′ precipitates and consequently contributed to chemical composition change near the γ/γ′ interface and its mobility.

Upon preheating and rapid cooling, dislocation movement took place and their density in the microstructure increased. This was, in the absence of the applied external stresses, caused by the material's tendency to relax structural stresses caused by, e.g., the change in γ/γ′ misfit parameter. Dislocation networks were formed to accommodate lattice misfit between the γ′ and γ phases (Fig. 3b). The images indicate that the variation in lattice parameters between the phases significantly affects the nature and morphology of the γ′ precipitates at the interface. Similar dislocations and dislocation lattices were not observed on cubic or fine spherical γ′ precipitates. The absence of these defects may be the result of lower γ/γ′ lattice misfit stresses. Stacking faults were also observed inside the matrix channels and on partially dissolved secondary γ′ precipitates. Stacking faults occurred in large secondary γ′ precipitates, possibly caused by dislocation slips in the γ′ phase. Differences in deformation mechanism between large and small γ′ precipitates can also be seen. The M_5B_3 boride nanoprecipitates strengthening the γ/γ′ interfaces in initial condition were still stable at 1100 °C. In this case, they constitute a barrier to the γ/γ′ interfacial boundary that moves during dissolution. Complete dissolution of the primary γ′ precipitates was not achievable at 1100 °C, even during long-term annealing, as they had formed at higher

Figure 3 Changes in the γ' precipitates morphology and structural defects occurring after the preheating at 1100 °C: **a** nanoprecipitates and single dislocations at the secondary γ/γ' interface; **b** dislocations network at the γ/γ' interface; **c** dislocations at the primary γ'/matrix interface; **d** lack of coherency between MC carbides and surrounding it secondary γ', TEM-BF.
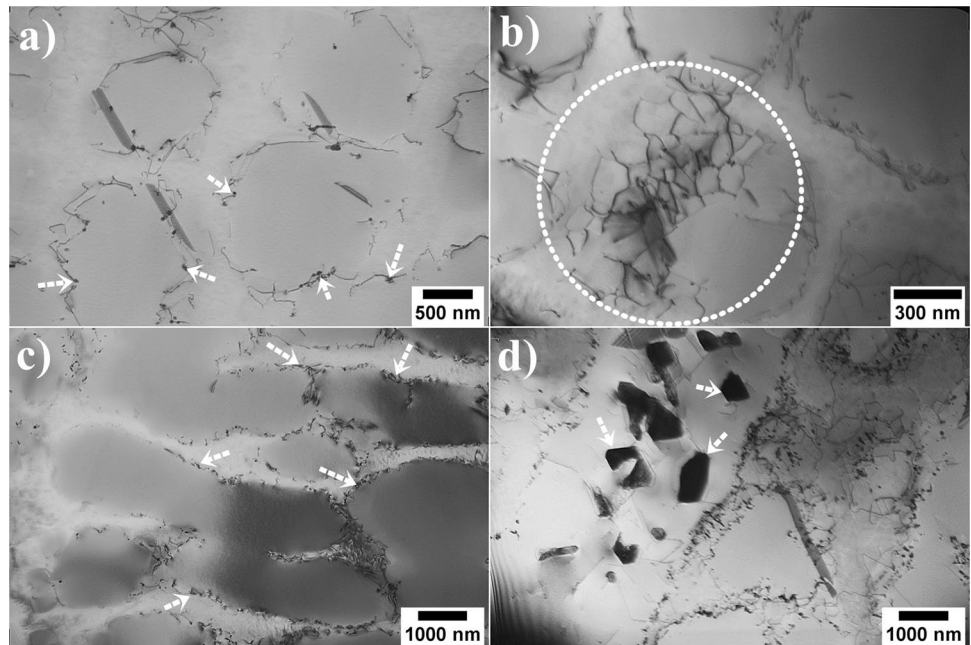

temperatures. Numerous dislocations are observed at γ/γ' interfaces, indicating structural stresses originating from lattice misfit (Fig. 3c). The secondary γ' precipitates, like the dendritic regions, exhibit numerous dislocation networks and stacking faults. The density of dislocations in the interdendritic spaces appears to be higher than in dendrite cores, suggesting a higher γ/γ' misfit coefficient. Defects, such as dislocation networks and stacking faults between the carbides and the γ phase, are not evident due to the lack of coherence (Fig. 3d). In their initial state, coarse-grained secondary γ' precipitates also surround less morphologically complex MC carbides (elongated parallelograms) (Fig. 4a). Preheating at 1100 °C led to partial dissolution of the γ' precipitates, which was initiated

at the MC/γ' interface and proceeded toward the outer edges (Fig. 4b). Between carbides, fine γ' precipitates surrounded by a γ matrix, formed during cooling after preheating, were observed. No others secondary precipitates were found in this area.

Large secondary γ' precipitates surround the Chinese script MCs and adhering $M_{23}C_6$ nano-carbides in aged condition. Preheating at 1100 °C resulted in a significant dissolution of the γ' precipitates, as confirmed by SEM-BSE images. Locally, as a result of large secondary γ' precipitate partial dissolution surrounding MC carbides, fine γ' precipitates precipitated from the supersaturated matrix during cooling. The $M_{23}C_6$ carbides adhering to MC carbides completely dissolved. Their initial thickness (visible on a thin foil) was only

Figure 4 a Coarse-grained secondary γ' precipitate morphology changes due to partial dissolution; **b** distribution of Cr, Hf and Ni in partially dissolved γ' precipitates and MC carbides, STEM-EDX.
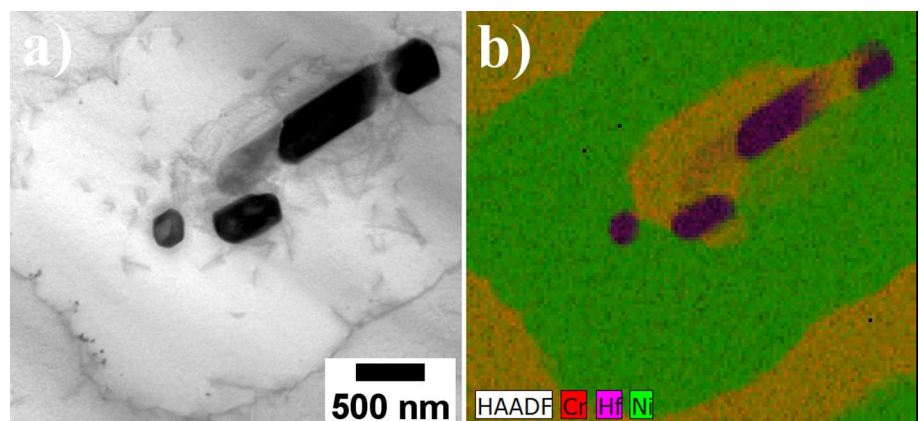
a few to a dozen nanometers [21], indicating that even the short holding time was sufficient for them to dissolve fully. This proves that the typical phase transformation $MC + \gamma \rightarrow M_{23}C_6 + \gamma'$ (leading to $M_{23}C_6$ nano-carbides formation) may be reversible. While observing MC carbides with Chinese script morphologies, fine spherical precipitates with a diameter of about 500 nm were found (Fig. 5). STEM-EDX showed that these precipitates are enriched in W, Cr and Mo. Based on FFT images (Fig. 6a–b), the precipitates were identified as M_5B_3 borides; therefore, their chemical formula will be $(Cr, W, Mo)_5B_3$. Boron may partially replace carbon in the crystal lattice of $M_{23}C_6$ carbides, so the source of B could be dissolved carbides. Precipitates having a $D8_1$ (M_5B_3) tetragonal lattice structure

were further analyzed via electron energy loss spectroscopy (EELS). The secondary precipitates formed after the preheating cycle were boron-rich (Fig. 6c). The signal from the K shell was recorded at an energy of approximately 190 eV. No corresponding signal at 284 eV, which would indicate the presence of carbon, was observed. This suggests the precipitates being borides rather than carbide–borides.

Fine precipitates (100–200 nm) remained along the grain boundaries even after preheating at 1100 °C (Fig. 7a–b). Chemical composition analyses indicated enrichment in Cr, characteristic of M_5B_3 borides and $M_{23}C_6$ carbides (Fig. 7c). To unambiguously identify the precipitates, HAADF-STEM images were subjected to FFT (Fig. 7d). The distribution of reflections
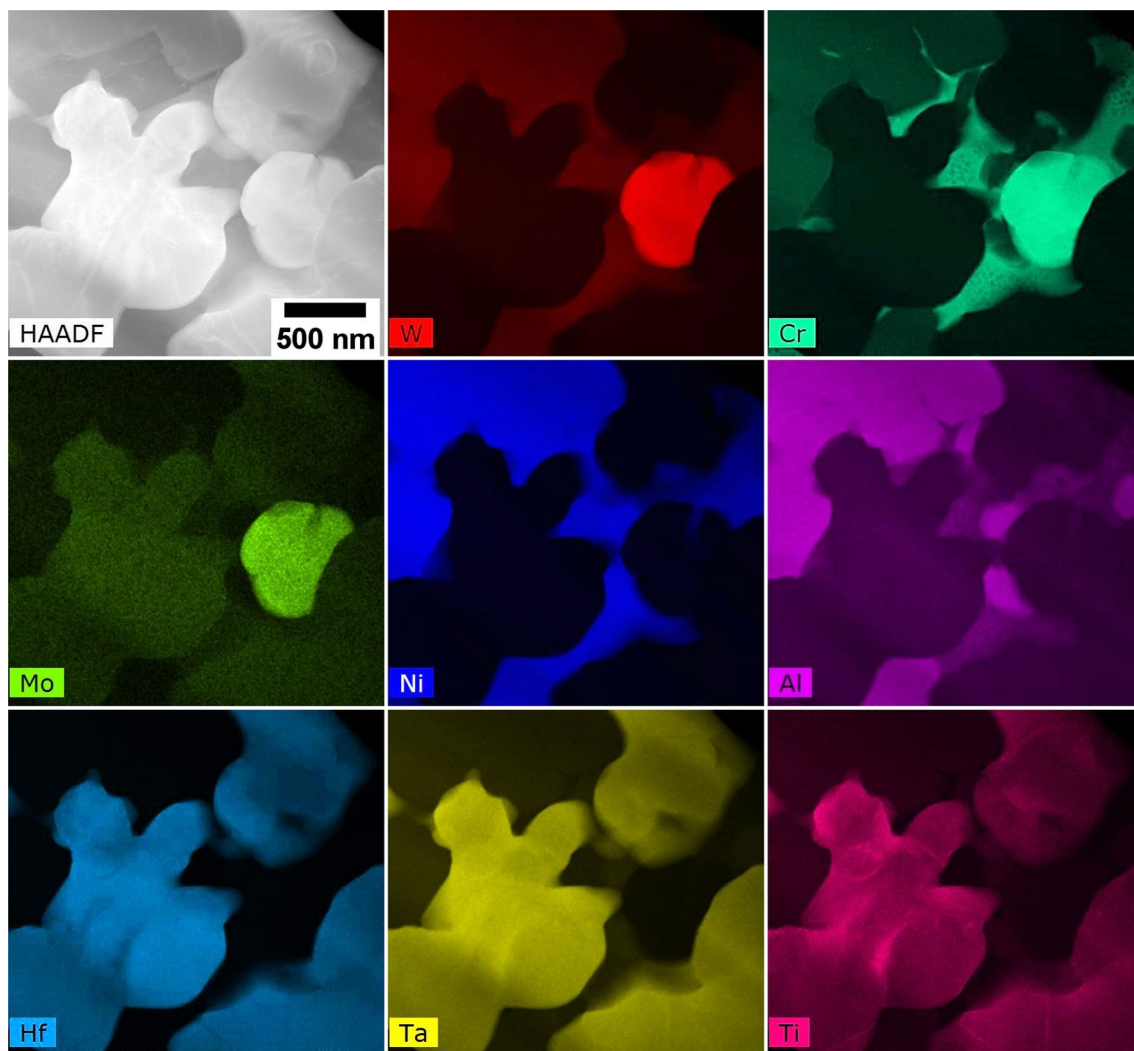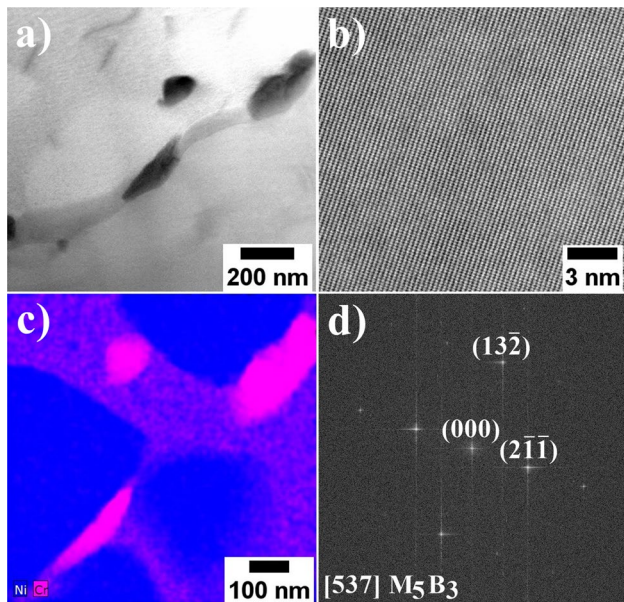

Figure 5 Morphology of partially dissolved secondary γ' precipitates surrounding MC carbides and secondary M_5B_3 borides (STEM-HAADF), as well as the distribution of selected alloying elements, STEM-EDX.
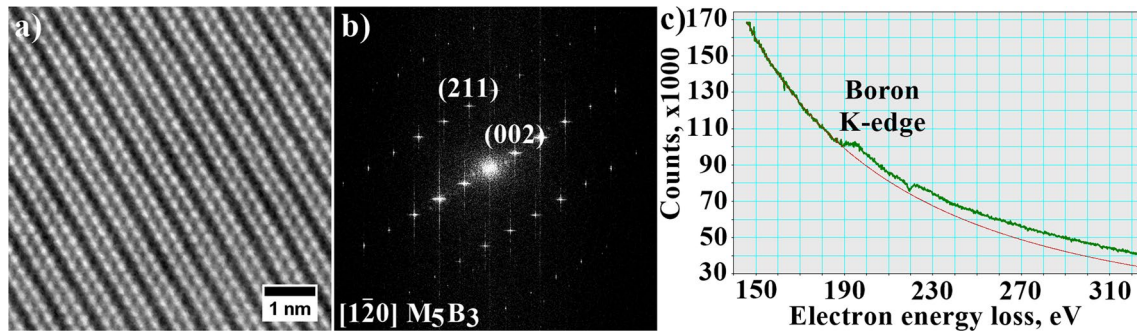
Figure 6 a–b Atomic-scale resolution STEM-HAADF imaging and calculated FFT image; **c** STEM-EELS of M_5B_3 borides.

Figure 7 a–b morphology and nanostructure of M_5B_3 precipitates at grain boundaries; **c** distribution of Ni and Cr; **d** M_5B_3 boride nanostructure and diffraction pattern calculated via FFT, STEM-HAADF.

on the calculated diffraction pattern suggests the presence of tetragonally structured M_5B_3. The formation of a non-equilibrium liquid layer may be favored by other factors, apart from constitutional liquation of only γ′ precipitates. M_5B_3 borides play an important role in the propagation of liquation cracks along grain boundaries [22]. The boron atom is larger than carbon and nitrogen and smaller than the substitution atoms dissolved in the matrix (Co, Cr). From the energetic point of view, boron segregation to areas with looser packing of atoms, e.g., grain and interfacial boundaries, is beneficial. During welding, M_5B_3 borides could have dissolved along the grain boundaries, increasing B concentration at the M_5B_3/γ interface.

Boron enrichment of the matrix is associated with a local decrease in melting point. Boron is also a surface-active element. It improves the wettability of the interdendritic liquid by lowering the free energy at the solid–liquid interface [23]. When tensile stresses increase, the material weakens during welding, especially in the final stage of liquid solidification. L. O. Osoba [24], based on weldability tests of the Haynes 282 superalloy, showed that constitutional liquation of M_5B_3 borides was the main reason for liquation cracks. To eliminate the harmful effects of borides, the Haynes 282 superalloy was annealed in the range of 1050–1150 °C for 2 h. The M_5B_3 borides remained stable at 1050 °C, with initial dissolution observed at 1080 and 1100 °C. At 1120 °C, borides were no longer found in the Haynes 282 superalloy.

Microstructure changes in HAZ after welding with the induction preheating

The cross section microstructure of the preheated René 108 superalloy after autogenous bead-on-weld is shown in Fig. 8. The fusion zone (FZ) was free from hot solidification cracks and other imperfections. Despite significant microstructural changes described in previous chapter, liquation cracks were still present in samples preheated to $T_0 = 900$ and 1000 °C. Their number and maximum length were smaller compared to the non-preheated variant [16]. However, total crack elimination was not achieved for the studied T_0 temperatures. The most promising results were obtained for samples preheated to 1100 °C, as no liquation cracks were observed in the LM images. Selected regions were subjected to further observations to analyze the mechanism of crack formation and the morphology of newly formed precipitates on their edges (Figs. 10, 11 and 12).

Figure 8 Microstructure changes in HAZ after autogenous welding with preheating to the temperature: **a** 900 °C; **b** 1000 °C; **c** 1100 °C. Arrows indicate microcracks in HAZ, LM.
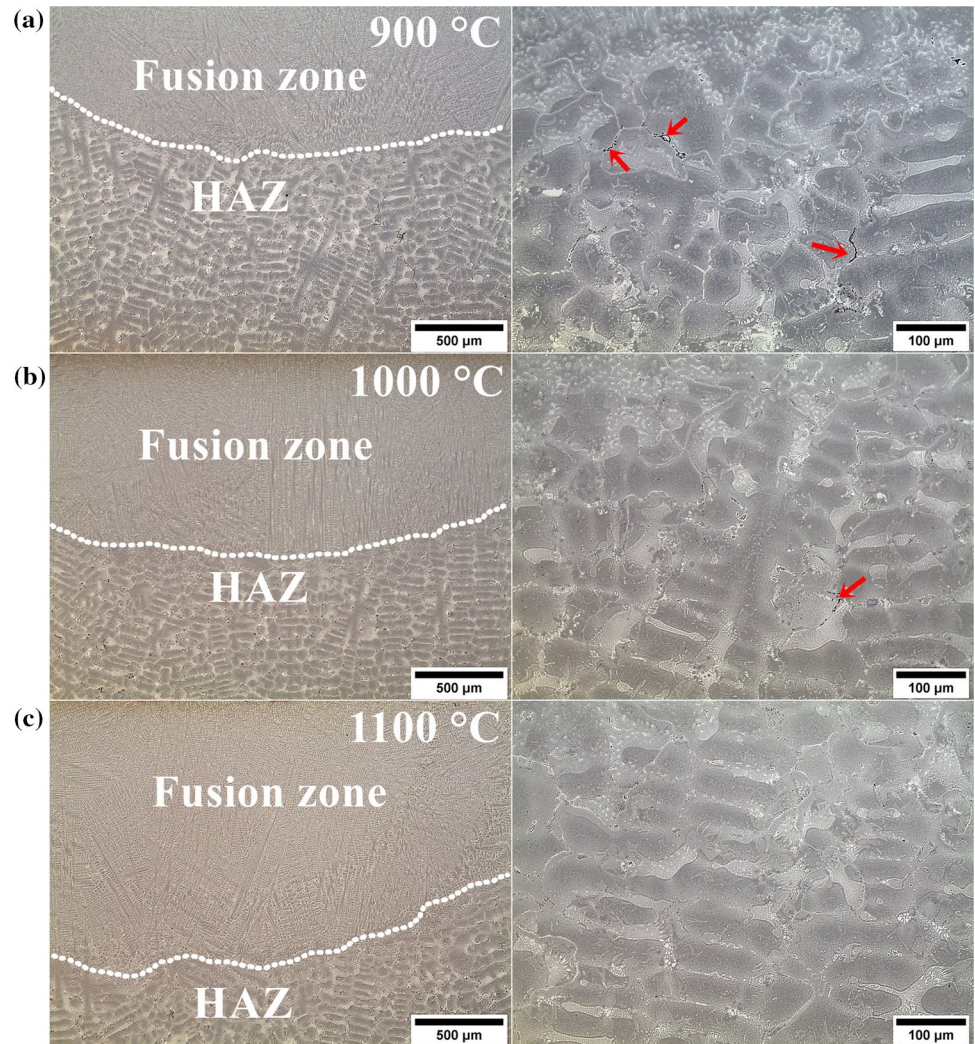
In the sample preheated to 900 °C, several micrometers long microcracks were locally observed along grain boundaries in the HAZ (Fig. 9a–c). The liquid phase necessary for initiating liquation cracks was formed mainly via constitutional liquation of γ' precipitates. The heat introduced during preheating and subsequent bead-on-plate autogenous welding also led to constitutional liquation of the γ' precipitates in areas far away from the grain boundaries. This is related to their lower (compared to the surrounding area) local solidus temperature. Secondary γ' precipitates in the dendritic regions and interdendritic spaces were mainly dissolved during the process, however, not melted. During cooling after welding, they re-precipitated from the supersaturated γ matrix. MC carbides were formed locally along the edges of the liquation cracks; however, their contribution to forming the non-equilibrium liquid during

welding is presumed to have been negligible. Tantalum and hafnium carbides are characterized by the highest melting point among MC carbides (3900 and 3880 °C) and low chemical reactivity [25]. $M_{23}C_6$ nano-carbides may have had a greater contribution, as they are metastable and start to dissolve above 950 °C, while above 1010–1040 °C are completely dissolved in the γ matrix [26]. Additionally, as concluded based on observation (Figs. 5 and 9d), the reaction $M_{23}C_6 + \gamma' \rightarrow MC + \gamma$ may have had occurred at high temperatures, which was also observed by Sims [27]. The presence of the γ phase near MC carbides (initially having a core–shell morphology) is significant from the weldability point of view as it enabled the constitutional liquation of the γ' phase surrounding these carbides. In many regions, strengthening precipitates inhibited the development liquation cracks. Single micro-fissures separated by healed cracks most

Figure 9 HAZ microstructure after bead-on-plate autogenous welding with preheating to 900 °C: **a** selected areas A and B with liquation microcracks; **b–c** morphology of newly formed γ–γ' eutectic precipitates on the edge of liquation fractures in areas A and B; **d** the liquation crack in the core–shell morphology location; **e** LFM zone near the microcracks; **f** LFM zone near healed microcrack; **g–h** cracks healed by the liquid formed via constitutional liquation, SEM-BSE.
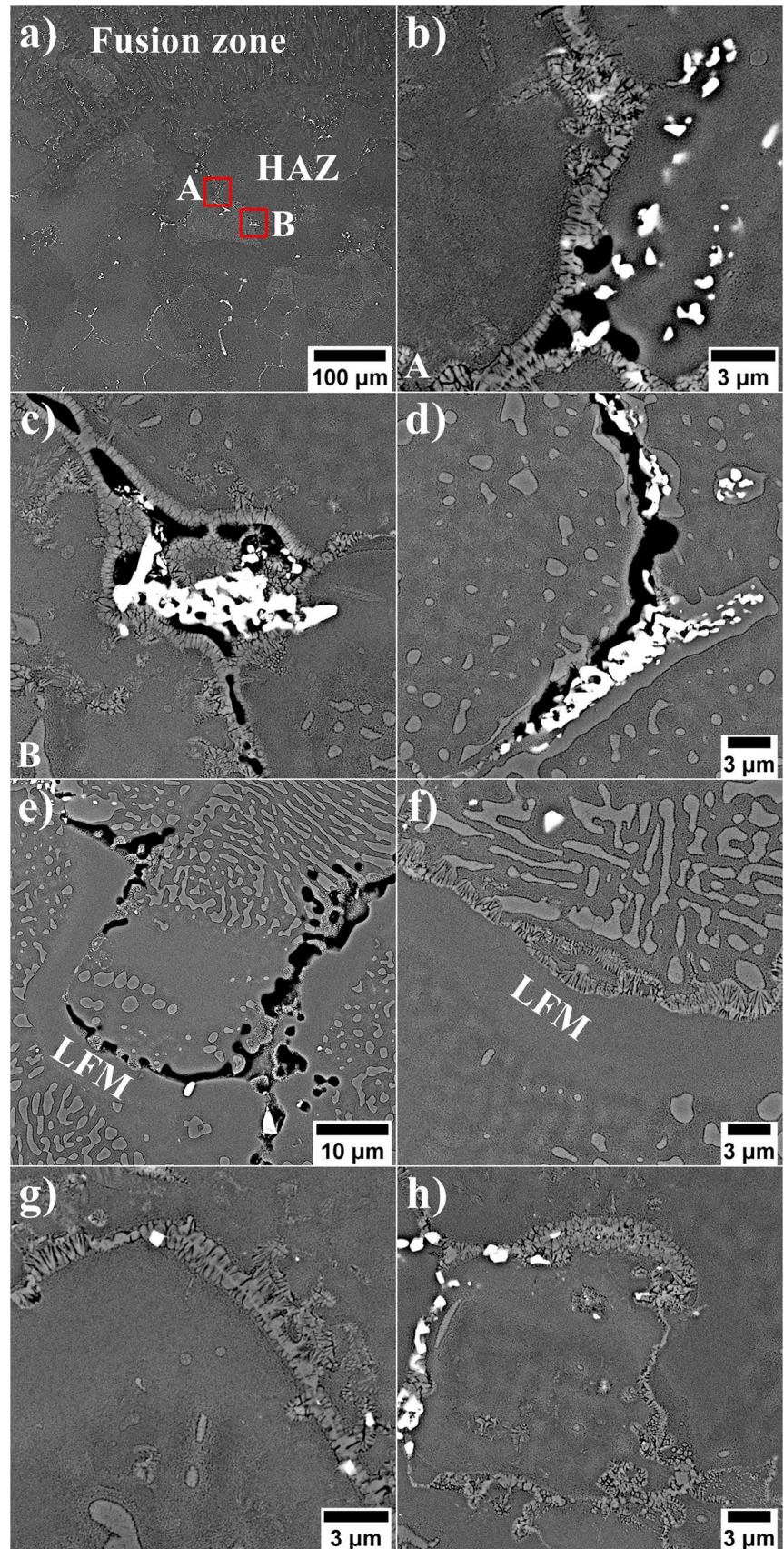
likely resulted from local fluctuations in chemical composition. These differences determine the start temperature of constitutional liquation. M_5B_3 borides at the grain boundaries may additionally contribute to lowering this temperature. Boron belongs to group of surface-active elements, similarly like zirconium and sulfur, and decrease the solid–liquid interfacial energy, which significantly aids wetting properties [28]. Complete dissolution of γ' precipitates in Ni-based superalloys (without the risk of constitutional liquation) is possible when the heating rate is in the range of 0.03–0.16 °C/s [29]. Meanwhile, the heating rate during arc welding of the Inconel 738LC superalloy is usually around 150 °C/s [30]. This indicates that most often it is constitutional liquation that facilitates liquid phase formation, suggesting that the key to improving weldability is focusing on the material's behavior during subsequent cooling. Solidification of a thick layer of interdendritic liquid through eutectic transformation may result in an extension of the high-temperature brittleness range, with a simultaneous increase of stresses near grain boundaries. This is one of the sources of superalloy weldability problems. The metastable liquid formed via constitutional liquation reacted with neighboring grains due to the back diffusion of dissolved elements. This takes place through the liquid/solid interface, resulting in the non-equilibrium interfacial energy being lowered and facilitating grain boundary wetting and liquid penetration, as observed on the microstructure. Not enough liquid volume and high stresses led to easy microcrack development. The arrangement (appreciable GB curvature) and the amount of grain boundaries, on which a non-equilibrium thin liquid film formed, show that the susceptibility to constitutional liquation is still high. However, the number of observed microcracks decreased with preheating. During cooling after bead-on-plate autogenous welding, the solid phase nucleated epitaxially on partially melted HAZ grains. It solidified as γ–γ' eutectic. Locally, liquid film migration (LFM) zones were observed, the presence of which indicates solidification via liquid migration (Fig. 9e). Some of them prevented the formation of a crack gap, which suggests their positive effect on reducing crack susceptibility, also in the variant with preheating to 900 °C (Fig. 9f). The solidification rate of the non-equilibrium liquid film in the HAZ, formed via LFM, is higher than for eutectic solidification and can increase the fracture toughness of the superalloy. This ensures relatively high strength during material

cooling under simultaneously increasing tensile stresses. It is expected that the liquid solidification process induced via LFM is related to the thickness of the liquid layer formed during heating upon welding at the grain boundaries [31]. According to Barker [32], the time needed for the liquid to solidify can be presented as the ratio of the layer thickness and the initial migration rate. Increasing the thickness of the liquid thin film causes a decrease in the initial migration velocity and increases the time required for the liquid to solidify only via migration (omitting eutectic-type solidification). This time is extremely limited as high cooling rates accompany welding processes, which is why observed re-solidification products are both in eutectic and LFM zones. At many grain boundaries, where the liquid volume during welding was sufficiently large, microcrack self-healing occurred (Fig. 9g–h). Crack self-healing occurred along grain boundaries reinforced with MC carbides and γ' phase precipitates, on which MC carbides were not observed. Ojo [31] indicated that in solid–liquid systems, high surface free energy at grain boundaries favors their wetting by the liquid phase. Wide-angle boundaries with a large angle of disorientation are high-energy areas, so the liquid spreads easily along them.

Applying a preheating temperature of 1000 °C further reduced the superalloy's susceptibility to liquation cracking (Fig. 10a–b), with fewer and smaller microcrack observed in comparison to 900 °C (Fig. 10c). The higher temperature facilitated creating greater amounts of non-equilibrium liquid film at the grain boundaries, in turn reducing thermal stresses. If the liquid volume is too low and there is a lack of free circulation, then the liquid cannot fill all the generated microcracks. Especially in the case when some cracks acted as fine voids (a few microns in length). As in the case of preheating at 900 °C, the γ' phase was mainly constitutionally liquated, most probably along with some amounts of M_5B_3 and $M_{23}C_6$ (Fig. 10d). The γ–γ' eutectic crystallized along the liquated crack edges, exhibiting the same morphological features. Local liquid solidification via migration is evidenced by numerous LFM zones, some of which helped to prevent to microcrack formation (Fig. 10e). There were areas within the HAZ, where the liquid had formed via constitutional liquation and had a sufficiently large volume and ease of circulation to inhibit micro-fissures development (Fig. 10f–h). MC carbides at grain boundaries also effectively blocked crack propagation. Inside the grains, the secondary γ' precipitates were

Figure 10 HAZ microstructure after welding with preheating to 1000 °C: **a–b** single microcracks and morphology of newly formed γ–γ' eutectic; **c** microcracks in close proximity to the LFM zone and γ–γ' eutectic; **d** liquation cracking in the core–shell morphology region; **e** LFM zones at liquated grain boundaries; **f–h** self-healing of cracks in locations C and D, SEM-BSE.
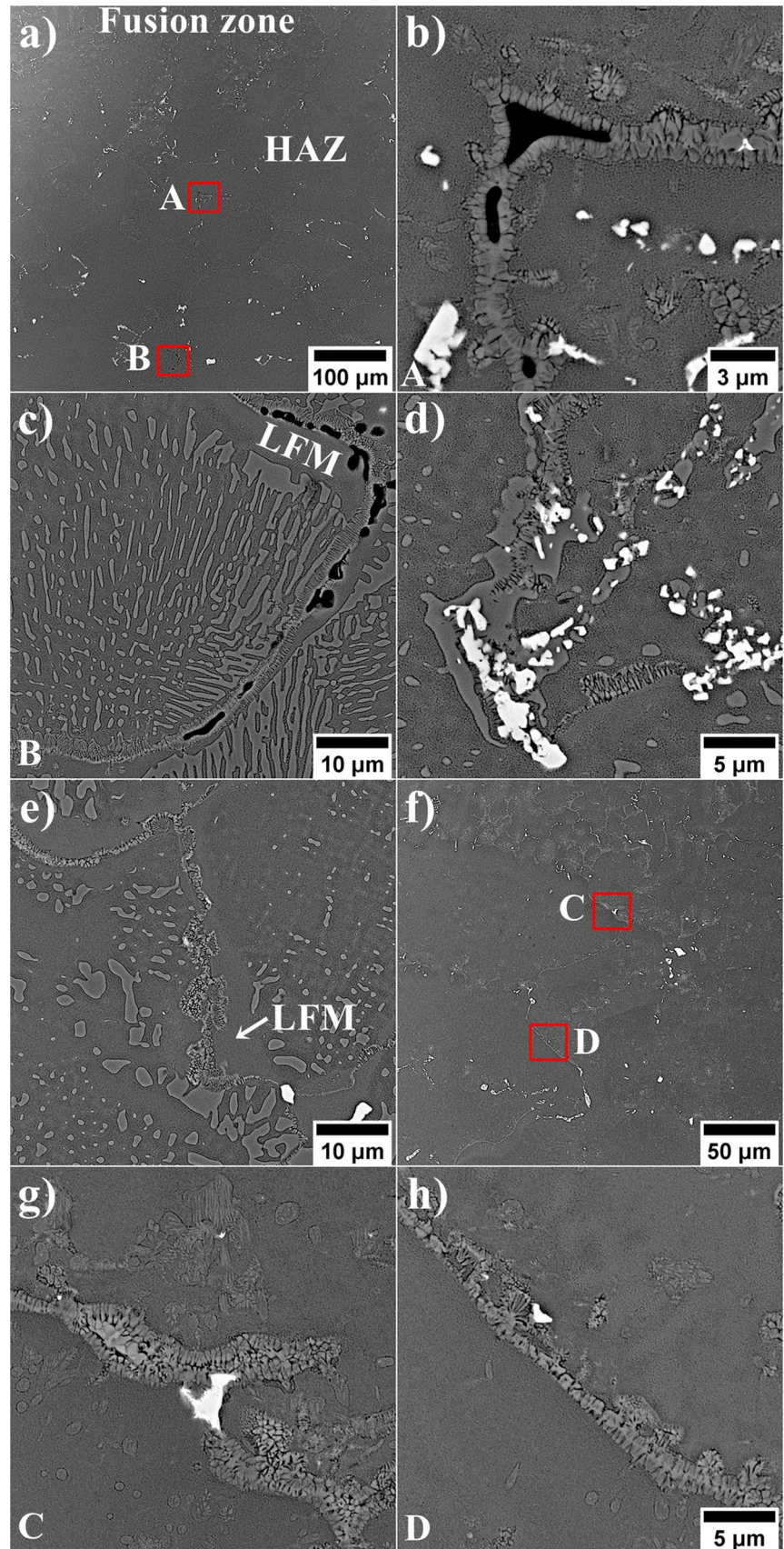
dissolved to a greater extent, which resulted from the higher preheating temperature.

Preheating to 1100 °C enabled eliminating liquation cracks in the HAZ (Fig. 11a). The increase in preheating temperature contributed to the dissolution of more γ' precipitates and the formation of a significant volume of non-equilibrium liquid. Constitutional liquation of the γ' precipitates took place at the grain boundaries, as well as locally in areas adjacent to these boundaries (Fig. 11b–d). The newly formed eutectic γ–γ' layer on the grain boundaries, originating from the non-equilibrium liquid, had a different thickness, most likely related to the local change in chemical composition (Fig. 11e–g). No relationship was observed between the thickness or morphology of the newly formed eutectic γ–γ' and the distance from the fusion line, where the temperature during welding was the highest among all HAZ areas. The liquated grain boundaries were locally accompanied by LFM zones (Fig. 11h), similarly as in the case of lower preheating temperatures (900 and 1000 °C). The crystallization of the non-equilibrium liquid layer via LFM effectively improved fracture toughness.

During Gleeble experiments on Renè 108 at high temperatures, eutectic γ–γ' with a morphology indicating local constitutional liquation was observed in samples heated to 1150 °C, which is 144 °C lower than the incipient melting determined during differential scanning calorimetry [16]. This means that constitutional liquation can even take place in samples preheated to 1100 °C. The obtained results are consistent with those presented by Ojo [31], who subjected the Inconel 738LC nickel superalloy to Gleeble tests at 1140, 1165, 1180 and 1245 °C (heating rate: 150 °C/s). Microstructural changes, being the sign of the beginning of constitutional liquation, were observed at 1165 °C. At two successive temperatures, numerous precipitates with a morphology typical of γ–γ' eutectics were found on crack edges. Osoba [24], based on Gleeble tests of the Haynes 282 superalloy, showed that M_5B_3 borides could also melt in a similar temperature range. At 1150 and 1170 °C, constitutional liquation of M_5B_3 borides occurred, while (Ti, Mo) C carbides were still stable. To limit superalloy susceptibility to liquation cracking, heat treatment at 1080–1100 °C was proposed before welding. Heat treatment at this temperature was sufficient to dissolve the M_5B_3 borides along the grain boundaries, improving the weldability of the Haynes 282 superalloy. Li [33] observed the first signs of sintering in the

Inconel 617B superalloy at 1250 °C, while the solidus temperature of this alloy is 1368 °C [34]. The phase responsible for the appearance of the non-equilibrium liquid was partially dissolved $M_{23}C_6$ carbides. Despite constitutional liquation of $M_{23}C_6$ carbides during GTA welding, liquation cracks did not form in the microstructure. This indicates that a sufficiently high-stress level is also required to initiate micro-fissuring.

Thin foils were collected from the area of re-solidification products γ–γ' via FIB-SEM, perpendicularly to the surface observed on the SEM-BSE images (Fig. 12). The region was analyzed and the LFM zone, M5B3 at grain boundaries, and primary blocky-shaped MC carbides were identified. The TEM-BF images show that crack-healing occurred along the entire grain boundary and can contribute to improving weldability. Neither micro-fissures nor voids were present. The eutectic γ–γ' phase formed from non-equilibrium liquid during cooling after welding was detected via selected area electron diffraction (SAED). Shrinkage during solidification is a source of stress affecting the heat-affected zone. According to Miller [35], the critical level of tensile stress (σ) exceeding the value of the surface tension at the solid/liquid interface (γ_{SL}) at the grain boundary containing a thin liquid layer of thickness (h) is determined by the relation $\sigma = 2\gamma_{SL}/h$. Increasing the thickness of the liquid film at the grain boundary can reduce the stress required for decohesion at the solid/liquid interface. However, the alloy's tendency to liquation cracking does not increase proportionally with liquid layer thickness, as the above-mentioned relationship would indicate. The limiting thickness is the one that guarantees the start of the self-healing process, which in turn prevents the propagation of microcracks. The concept of self-healing was introduced by Vero [36], who stated that in the initial stage of solidification, the interdendritic liquid layer could fill the microcracks between the crystallites and thus stop their further development. When the volume of the liquid phase during solidification exceeds a specific critical value, a liquid stream will fill each of the created gaps. The liquid required to achieve a complete healing effect may vary from alloy to alloy. Clyne [37] suggested that the liquid volume should locally reach at least 10%. Microcrack self-healing with eutectic liquid has also been reported for corrosion-resistant steels, where their tendency to hot cracking during the Trans-Varestraint test was studied [38]. In comparison, when

Figure 11 HAZ microstructure after welding with preheating to 1100 °C: **a** crack-free HAZ; **b** location of areas A and B along grain boundaries; **c–d** effective self-healing of liquation cracks with eutectic at the grain boundary; **e** location of areas C and D; **f–g** difference in the thickness of the newly formed eutectic γ–γ' at the grain boundary; **h** LFM zone accompanying the melted grain boundary, SEM-BSE.
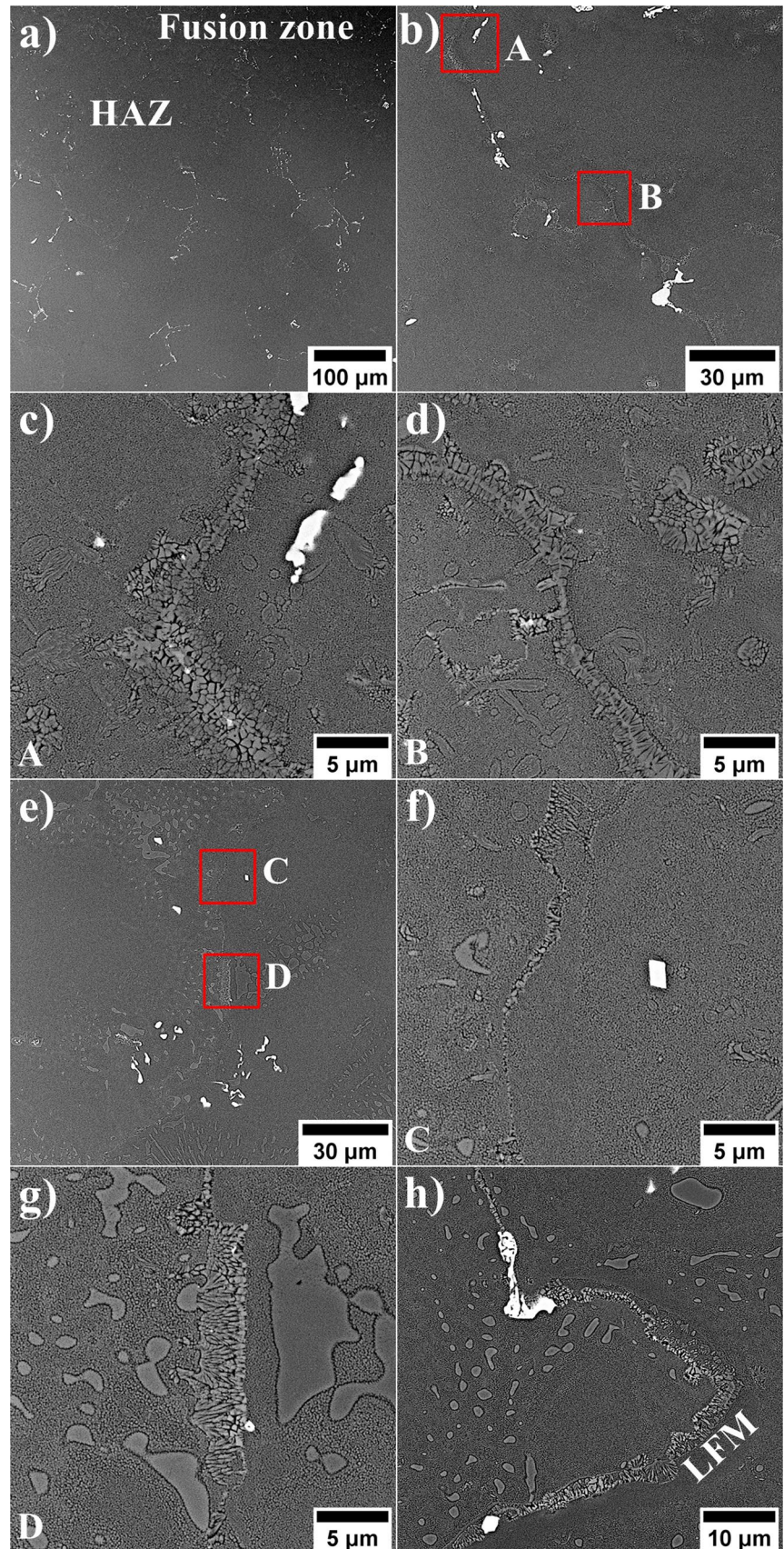
Figure 12 **a** Liquation crack self-healing at grain boundaries; **b** LFM zone and M$_5$B$_3$ at GBs; **c** morphology of the newly formed γ–γ' eutectic; **d** SAED of the newly formed γ–γ' eutectic at GBs, TEM.
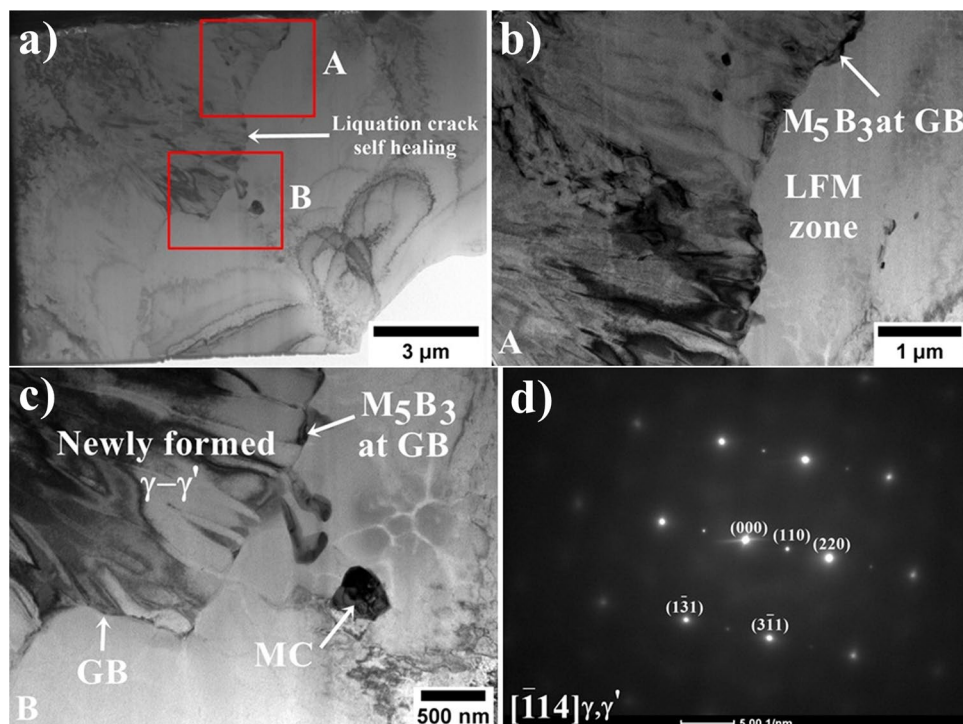
weldability of aluminum alloys was investigated, it was found that the total crack length increased with increase in amounts of eutectic liquid. Only after reaching a certain volume of liquid in the interdendritic areas was the formation and propagation of cracks reduced [28].

Conclusions

This work focused on analyzing the effects of induction preheating on the improvement of the René 108 superalloy's resistance to liquation cracking in HAZ during gas tungsten arc welding. The main conclusions are as followed:

1. The dissolution of γ' phase precipitates occurred during preheating. The volume fraction of secondary γ' precipitates in the dendritic regions gradually decreased from 52% at 900 °C to 34% at 1100 °C. The mean size of the secondary γ' decreased from 0.32 to 0.26 μm.
2. During preheating, the M$_{23}$C$_6$ carbides located at the edges of MC carbides completely dissolved. In these areas, secondary M$_5$B$_3$ boride precipitates

were observed, which remained stable at γ/γ' interfaces and along grain boundaries.
3. The application of a preheating step prior to autogenous bead-on-weld via GTAW allowed to obtain fusion zones free of hot solidification cracks.
4. A sufficiently high preheating temperature (T_0 = 1100 °C) could contribute to the elimination of liquation cracks through intensified γ' precipitate dissolving, thermal stress reduction and microcrack self-healing with a liquid eutectic.
5. A thin layer was observed along crack edges, indicating that a liquid phase was locally present at elevated temperatures. Rapid heating above the γ' solvus temperature led to the formation of eutectic liquid due to the reaction of partly dissolved γ' precipitates with the matrix. The location of the cracks suggests that M$_5$B$_3$ borides and M$_{23}$C$_6$ carbides could have participated in constitutional liquation. It was found that the role of MC carbides in increasing susceptibility to liquation cracking is not significant.

Acknowledgements

Author contributions

ŁR contributed to conceptualization, provided methodology, carried out Preludium 13 project administration, wrote the original manuscript, performed welding tests, carried out SEM observations and analyses. MGR performed welding experiments, carried out LIDER project administration and edited the manuscript. BR performed STEM, STEM-EDX and EELS experiments and data analysis, and edited the manuscript. RC provided resources, supervised and edited the manuscript. AZL performed TEM observations, supervised and edited the work.

Data and code availability

Not applicable.

Declarations

Conflict of interest The authors declare that they have no known competing financial interests or personal relationships that could have appeared to influence the work reported in this paper.

Ethical approval This article does not contain any studies with human participants or animals performed by any of the authors.

References

[1] Hanning F, Andersson J (2018) Weldability of wrought Haynes® 282® repair welded using manual gas tungsten arc welding. Weld World 62:39–45. https://doi.org/10.1007/s40194-017-0508-z

[2] Rogalski G, Świerczyńska A, Landowski M, Fydrych D (2020) Mechanical and microstructural characterization of tig welded dissimilar joints between 304l austenitic stainless steel and Incoloy 800HT nickel alloy. Met 20(2):559. https://doi.org/10.3390/met10050559

[3] Sazerat M, Nait-Ali A, Cervellon A, Lopez-Galilea I, Burlot G, Gillet S, Eyidi D, Joulain A, Villechaise P, Weber S, Fortunier R, Cormier J (2023) High temperature microstructure stability of Waspaloy produced by wire arc additive manufacturing. J All Comp 966(5):171626. https://doi.org/10.1016/j.jallcom.2023.171626

[4] Agilan M, Venkateswaran T, Sivakumar D, Pant B (2014) Effect of heat input on microstructure and mechanical properties of Inconel-718 EB welds. Proc Mat Sci 5:656–662. https://doi.org/10.1016/j.mspro.2014.07.312

[5] Ojo O, Richards N, Chaturvedi M (2004) Contribution of constitutional liquation of gamma prime precipitate to weld HAZ cracking of cast Inconel 738 superalloy. Scri Mater 50:641–646. https://doi.org/10.1016/j.scriptamat.2003.11.025

[6] Hanning F, Khan AK, Andersson J, Ojo O (2020) Advanced microstructural characterisation of cast ATI 718Plus®—effect of homogenisation heat treatments on secondary phases and repair welding behaviour. Weld World 64:523–533. https://doi.org/10.1007/s40194-020-00851-0

[7] David SA, Siefert JA, DuPont JN, Shingledecker JP (2015) Weldability and weld performance of candidate nickel base superalloys for advanced ultrasupercritical fossil power plants part I: fundamentals. Sci Tech Weld Join 20(7):532–552. https://doi.org/10.1179/1362171815Y.0000000035

[8] Gudivada G, Pandey AK (2023) Recent developments in nickel-based superalloys for gas turbine applications: review. J All Comp 963:171128. https://doi.org/10.1016/j.jallcom.2023.171128

[9] Sirohi S, Pandey S, Świerczyńska A, Rogalski G, Kumar N, Landowski M, Fydrych D, Pandey C (2023) Microstructure and mechanical properties of combined GTAW and SMAW dissimilar welded joints between inconel 718 and 304L austenitic stainless steel. Metals 13:14. https://doi.org/10.3390/met13010014

[10] Alvarez Tejedor T, Singh R, Pilidis P (2013) Maintence and repair of gas turbine components. In: Jansohn P (eds) Modern gas turbine systems. Woodhead Publishing, UK, pp 565–634. https://doi.org/10.1533/9780857096067.3.565

[11] Chen Y, Wang W, Ou Y, Li D, Chang H, Wu Y, Yang R, Zhai Z, Li C (2023) Effect of high preheating on the microstructure and mechanical properties of high gamma prime Ni-based superalloy manufactured by laser powder bed fusion. J All Comp 960:170598. https://doi.org/10.1016/j.jallcom.2023.170598

[12] David SA, Vitek JM, Babu SS, Boatner LA, Reed RW (1997) Welding of nickel base superalloy single crystals. Sci Technol Weld Join 2(2):79–88. https://doi.org/10.1179/stw.1997.2.2.79

[13] Xu J, Lin X, Guo P, Hu Y, Wen X, Xue L, Liu J (2017) The effect of preheating on microstructure and mechanical properties of laser solid forming IN-738LC alloy. Mater Sci Eng A 691:71–80. https://doi.org/10.1016/j.msea.2017.03.046

[14] Hu YL, Lin X, Song K, Jiang XY, Yang HO, Huang WD (2016) Effect of heat input on cracking in laser solid formed DZ4125 superalloy. Opt Laser Technol 86:1–7. https://doi.org/10.1016/j.optlastec.2016.06.008

[15] Suharno B, Sugianto A, Butario RE, Widagdo D, Estriyanto Y, Harjanto B (2012) Advantage of SWET technique on joining Inconel 792 material. Glob J Res Eng 12(6):12–16

[16] Rakoczy Ł, Grudzień-Rakoczy M, Rutkowski B, Cygan R, Hanning F, Cios G, Habisch S, Andersson J, Mayr P, Zielińska-Lipiec A (2023) The role of the strengthening phases on the HAZ liquation cracking in a cast Ni-based superalloy used in industrial gas turbines. Archiv Civ Mech Eng 23:119. https://doi.org/10.1007/s43452-023-00659-x

[17] Chen Y, Prasathbabu R, Slater TJ, Bai M, Mitchell B, Ciuca O, Preuss M, Haigh SJ (2016) An investigation of diffusion-mediated cyclic coarsening and reversal coarsening in an advanced Ni-based superalloy. Acta Mater 110:295–305. https://doi.org/10.1016/j.actamat.2016.02.067

[18] Vogel F, Wanderka N, Matsumura S, Banhart J (2012) Early stages of decomposition within the γ′ phase of a Ni–Al–Ti model alloy. Intermetall 22:226–230. https://doi.org/10.1016/j.intermet.2011.11.011

[19] Grosdidier T, Hazotte A, Simon A (1998) Precipitation and dissolution processes in γ/γ′ single crystal nickel-based superalloys. Mat Sci Eng A 256:183–196. https://doi.org/10.1016/S0921-5093(98)00795-3

[20] Doi M (1996) Elasticity effects on the microstructure of alloys containing coherent precipitates. Prog Mater Sci 40(2):79–180. https://doi.org/10.1016/0079-6425(96)00001-1

[21] Rakoczy Ł, Rutkowski B, Grudzień-Rakoczy M, Cygan R, Ratuszek W, Zielińska-Lipiec A (2020) Analysis of γ′ precipitates, carbides and nano-borides in heat-treated Ni-based superalloy using SEM, STEM-EDX, and HRSTEM. Mater 13:4452. https://doi.org/10.3390/ma13194452

[22] Li X, Ou M, Wang M, Zhang L, Ma Y, Liu K (2021) Effect of boron addition on the microstructure and mechanical properties of K4750 nickel-based superalloy. J Mater Sci Techn 60:177–185. https://doi.org/10.1016/j.jmst.2020.02.079

[23] Després A, Antonov S, Mayer C, Tassin C, Verona M, Blandin JJ, Kontis P, Martin G (2021) On the role of boron, carbon and zirconium on hot cracking and creep resistance of an additively manufactured polycrystalline superalloy. Materialia 19:101193. https://doi.org/10.1016/j.mtla.2021.101193

[24] Osoba L (2012) A study on laser weldability improvement of newly developed Haynes 282 superalloy. PhD dissertation, University of Manitoba

[25] Perevislov S, Vysotin A, Shcherbakova O (2020) Studying the properties of carbides in the system ZrC–HfC, TaC–ZrC and TaC–HfC. IOP Conf Ser: Mater Sci Eng 848:012069. https://doi.org/10.1088/1757-899X/848/1/012069

[26] Sabol G, Stickler R (1969) Microstructure of nickel-based superalloys. Physica Status Solidi (B) 35:11–52. https://doi.org/10.1002/pssb.19690350102

[27] Sims C, Stoloff NS, Hagel WC (1987) Superalloys II: High-temperature materials for aerospace and industrial power. Wiley, New York

[28] Ojo O, Richards N (2012) Heat affected zone cracking in welded nickel superalloys. In: Chaturvedi M (eds) Welding and joining of aerospace materials. Woodhead Publishing, UK. https://doi.org/10.1533/9780857095169.1.142

[29] Sponseller D (1996) Differential thermal analysis of nickel-base superalloys. In: Kissinger R (ed) Superalloys. TMS (The Minerals, Metals & Materials Society), pp 259–270. https://doi.org/10.7449/1996/Superalloys_1996_259_270

[30] Ojo O (2004) On liquation cracking of cast Inconel 738LC superalloy welds. PhD dissertation, University of Manitoba

[31] Ojo O, Richards N, Chaturvedi M (1998) Liquid film migration of constitutionally liquated γ' in weld heat affected zone (HAZ) of Inconel 738LC superalloy. Scri Mater 51:141–146 https://doi.org/10.1016/j.scriptamat.2004.03.040

[32] Barker SW, Purdy G (1998) On liquid film migration in aluminium-copper alloys. Act Mater 46:511–524. https://doi.org/10.1016/S1359-6454(97)00267-X

[33] Li S, Li K, Hu M, Wu Y, Cai Z, Pan J (2020) The mechanism for HAZ liquation of nickel-based alloy 617B during gas tungsten arc welding. Metal 10:94. https://doi.org/10.3390/met10010094

[34] Liu W, Lu F, Yang R, Tang X, Cui H (2015) Gleeble simulation of the HAZ in Inconel 617 welding. J Mater Process Techn 225:221–228. https://doi.org/10.1016/j.jmatprotec.2015.06.001

[35] Miller W, Chadwick G (1967) On the magnitude of the solid/liquid interfacial energy of pure metals and its relation to grain boundary melting. Acta Metall 15:607–614. https://doi.org/10.1016/0001-6160(67)90104-6

[36] Vero J (1936) The hot-shortness of aluminum alloys. Metals Industry 48:431–434

[37] Clyne T, Davies G (1979) Comparison between experimental data and theoretical predictions relating to dependence of solidification cracking on composition. In: Solidification and casting of metals. Metals Soc, pp 275–278

[38] Arata Y, Matsuda F, Katayama S (1977) Solidification crack susceptibility in weld metals of fully austenitic stainless steels (Report II)—effect of ferrite, P, S, C, Si and Mn on ductility properties of solidification brittleness. Trans JWRI 6:105–116